CMES, vol.8, no.3, pp.259-270, 2005

Meshless Local Petrov-Galerkin Method for Stress and Crack Analysis in 3-D Axisymmetric FGM Bodies

J. Sladek[1], **V. Sladek**[1], **J. Krivacek**[1], **Ch. Zhang**[2]

Abstract: A meshless method based on the local Petrov-Galerkin approach is presented for stress analysis in three-dimensional (3-d) axisymmetric linear elastic solids with continuously varying material properties. The inertial effects are considered in dynamic problems. A unit step function is used as the test functions in the local weak-form. It is leading to local boundary integral equations (LBIEs). For transient elastodynamic problems the Laplace-transform technique is applied and the LBIEs are given in the Laplace-transformed domain. Axial symmetry of the geometry and the boundary conditions for a 3-d linear elastic solid reduces the original 3-d boundary value problem into a 2-d problem. The geometry of subdomains is selected as a toroid with a circular cross section in the considered (x_1, x_3)-plane. The final form of the local integral equations has a pure contour-integral character only in elastostatic problems. In elastodynamics an additional domain-integral is involved due to inertia terms. The moving least-squares (MLS) method is used for the approximation of physical quantities in LBIEs.

keyword: Meshless method, local weak-form, unit step function, moving least-squares approximation, Laplace-transform, functionally graded materials (FGMs), transient elastodynamics, crack problems

1 Introduction

Functionally graded materials (FGMs) possess continuously nonhomogeneous material properties. These materials have been introduced in recent years to benefit from the ideal performance of its constituents, e.g. high heat and corrosion resistance of ceramics on one side, and large mechanical strength and toughness of metals on the other side. In FGMs, the composition and the volume fraction of their constituents vary continuously with spatial coordinates. A review on various aspects of FGMs can be found in the monograph of Suresh and Mortensen (1998).

The solution of the boundary or initial boundary value problems for continuously nonhomogeneous solids requires advanced numerical methods due to the high mathematical complexity. Conventional computational methods with domain or boundary discretizations such as the finite element method (FEM) and the boundary element method (BEM) have their own drawbacks in dealing with such kind of problems. It is efficient to apply the conventional BEM mainly to problems where the fundamental solution is available. The pioneering applications of the BEM to axisymmetric elasticity in homogeneous materials begun in the mid 1970s with the works of Kermanidis (1975) and Cruse at al. (1977). Recently, Lacerda and Wrobel (2001) have presented a hypersingular boundary integral equations formulation for axisymmetric elasticity. However, for general nonhomogeneous and linear elastic solids, elastostatic and elastodynamic fundamental solutions are yet, to the best of the authors knowledge, still not available. One way to avoid this difficulty is the application of a parametrix or Levi function in lieu of the fundamental solutions [Mikhailov (2002)]. A parametrix describes the main part of the fundamental solutions correctly but does not necessarily satisfy the original differential equations.

In spite of the great success of the FEM and the BEM as accurate and effective numerical tools for the solution of boundary value problems with complex domains, there is still a growing interest in developing new advanced numerical methods. In recent years, meshfree or meshless formulations are becoming to be popular due to their high adaptivity and low costs to prepare input data for numerical analyses. A variety of meshless methods has been proposed so far [Belytschko et al. (1994); Atluri and Shen (2002)]. Many of them are derived from a weak-

---

[1] Institute of Construction and Architecture, Slovak Academy of Sciences, 84503 Bratislava, Slovakia

[2] Department of Civil Engineering, University of Siegen, D-57068 Siegen, Germany

form formulation on global domain [Belytschko et al. (1994)] or a set of local subdomains [Atluri and Shen (2002), Sladek et al. (2003a,b); Mikhailov (2002); Sellountos et al. (2005)]. In the global formulation background cells are required for the integration of the weak-form. In methods based on local weak-form formulation no cells are required and therefore they are often referred to as truly meshless methods. If a simple form is chosen for the geometry of the subdomains, numerical integrations can be easily carried out over them. The meshless local Petrov-Galerkin (MLPG) method is a fundamental base for the derivation of many meshless formulations, since trial and test functions can be chosen from different functional spaces. By using the fundamental solution as the test function, accurate numerical results can be obtained, which were reported in previous papers for 2-D problems in isotropic, homogeneous or continuously nonhomogeneous and linear elastic solids under static [Atluri et al. (2000); Sladek et al. (2000)] and dynamic loading conditions [Sladek et al. (2003a,b); Sellountos and Polyzos (2003)], and for 3-D problems in homogeneous isotropic and linear elastic solids under static and dynamic loads [Han and Atluri (2004a,b)].

In this paper the MLPG with a unit step function as the test function is applied for 3-d axisymmetric isotropic and linear elastic solids with continuously varying material properties. Axial symmetry of the geometry and the boundary conditions for a 3-d solid reduces the original 3-d boundary value problem into a 2-d problem. A 3-d axisymmetric body is generated by the rotation of the cross section around the axis of symmetry. Then, it is sufficient to analyze only that cross section which is covered by small circular sub-domains surrounding interior nodes randomly spread on the analyzed domain. Interior and boundary nodes are used for the spatial approximation of the displacements. The moving least-squares (MLS) scheme is applied here for this purpose. The MLPG yields a pure contour-integral formulation on local boundaries of subdomain for elastostatic problems, while in elastodynamics an additional domain-integral due to inertia terms is involved. The Laplace-transform is applied to eliminate the time variable. Then, the local boundary integral equations are derived in the Laplace-transformed domain. Several quasi-static boundary value problems have to be solved for various discrete values of the Laplace-transform parameter. The Stehfest's inversion algorithm is then applied to obtain the time-dependent solutions. The integral equations have a very simple nonsingular form. Moreover, both the contour and the domain integrations can be easily carried out on circular sub-domains. The boundary conditions on the global boundary are satisfied by collocation of the MLS-approximation expressions for the displacements at global boundary nodes.

To demonstrate the accuracy of the present method, numerical examples with simple and complex geometry are presented for static and dynamic loading cases.

2 Local boundary integral equations

Let us consider an isotropic and linear elastic 3-d axisymmetric body generated by the rotation of the planar domain Ω bounded by the boundary Γ around the axis of symmetry as shown in Fig.1. The equilibrium equations in elastodynamics can be expressed as

$$\sigma_{ij,j}(\mathbf{x},t) - \rho \ddot{u}_i(\mathbf{x},t) = -X_i(\mathbf{x},t) \qquad (1)$$

where $\sigma_{ij}(\mathbf{x},t)$ is the stress tensor, $X_i(\mathbf{x},t)$ is the body force vector, ρ is the mass density, $u_i(\mathbf{x},t)$ is the displacement vector, and the dots indicate the time derivatives. A comma denotes partial differentiation with respect to the spatial coordinates. An elastostatic problem can be considered formally as a special case of the elastodynamic one by omitting the acceleration term $\ddot{u}_i(\mathbf{x},t)$

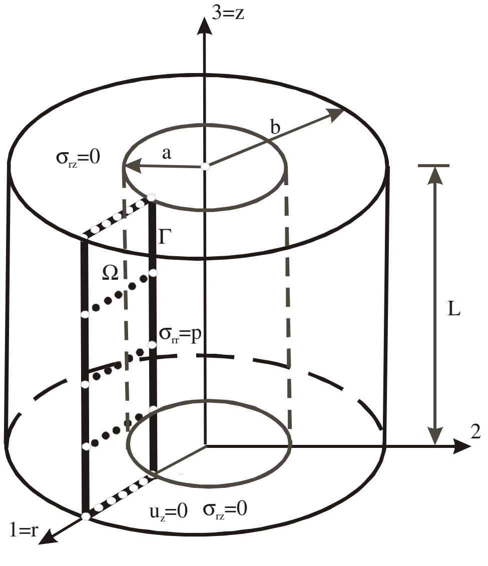

Figure 1 : Geometry of a 3-d axisymmetric body

in the equilibrium equations (1). Therefore, both cases are analyzed simultaneously in this paper.

For axisymmetric problem it is convenient to use cylindrical coordinates (r,φ,z). The angular component of the displacements vanishes and all physical fields are independent on the angular coordinate φ. In such a case the equilibrium equations have the following form

$$
\begin{aligned}
&\sigma_{rr,r}(r,z,t)+\sigma_{rz,z}(r,z,t)+\frac{1}{r}\left[\sigma_{rr}(r,z,t)-\sigma_{\varphi\varphi}(r,z,t)\right]\\
&\quad-\rho\ddot{u}_r(r,z,t)=-X_r(r,z,t),\\
&\sigma_{rz,r}(r,z,t)+\sigma_{zz,z}(r,z,t)+\frac{1}{r}\sigma_{rz}(r,z,t)-\rho\ddot{u}_z(r,z,t)\\
&\quad=-X_z(r,z,t)
\end{aligned}
\tag{2}
$$

where

$$
\begin{aligned}
&\sigma_{rr}=(2\mu+\lambda)u_{r,r}+\lambda\left(u_{z,z}+\frac{u_r}{r}\right),\\
&\sigma_{zz}=(2\mu+\lambda)u_{z,z}+\lambda\left(u_{r,r}+\frac{u_r}{r}\right),\\
&\sigma_{\varphi\varphi}=(2\mu+\lambda)\frac{u_r}{r}+\lambda\left(u_{z,z}+u_{r,r}\right),\\
&\sigma_{rz}=\mu\left(u_{z,r}+u_{r,z}\right)
\end{aligned}
\tag{3}
$$

Applying the Laplace-transform to the equilibrium equations (2), we have

$$
\begin{aligned}
&\overline{\sigma}_{rr,r}(r,z,p)+\overline{\sigma}_{rz,z}(r,z,p)+\frac{1}{r}\left[\overline{\sigma}_{rr}(r,z,p)-\overline{\sigma}_{\varphi\varphi}(r,z,p)\right]\\
&\quad-\rho p^2\overline{u}_r(r,z,p)=-\overline{F}_r(r,z,p)\\
&\overline{\sigma}_{rz,r}(r,z,p)+\overline{\sigma}_{zz,z}(r,z,p)+\frac{1}{r}\overline{\sigma}_{rz}(r,z,p)\\
&\quad-\rho p^2\overline{u}_z(r,z,p)=-\overline{F}_z(r,z,p)
\end{aligned}
\tag{4}
$$

where

$$
\begin{aligned}
\overline{F}_a(r,z,p)=&\,\overline{X}_a(r,z,p)+\rho(r,z)pu_a(r,z,0)\\
&+\rho(r,z)\dot{u}_a(r,z,0)
\end{aligned}
$$

is the redefined body force in the Laplace-transformed domain with the initial boundary condition for the displacements $u_a(\mathbf{x},0)$and the velocities $\dot{u}_a(\mathbf{x},0)$. Here, $a\in\{r,z\}$.

The Laplace-transform of a function $f(\mathbf{x},t)$ is defined as

$$
L[f(x,t)]=\overline{f}(x,p)=\int_0^\infty f(x,t)e^{-pt}d\tau
$$

where p is the Laplace-transform parameter.

Instead of writing the global weak-form for the above governing equations, the MLPG methods construct the weak-form over local subdomains such as Ω_s, which is a small region taken for each node inside the global domain [Atluri and Shen (2002)]. The local subdomains overlap each other, and cover the whole global domain Ω. The local subdomains could be of any geometric shape and size. In the present analysis, the local subdomains are taken to be of a circular shape. The local weak-form of the governing equations (4) on the subdomain Ω_s lying in the global domain Ω can be written as

$$
\begin{aligned}
&\int_{\Omega_s}\left(\overline{\sigma}_{rr,r}+\overline{\sigma}_{rz,z}\right)u^*d\Omega+\int_{\Omega_s}\frac{1}{r}\left(\overline{\sigma}_{rr}-\overline{\sigma}_{\varphi\varphi}\right)u^*d\Omega\\
&\quad-\int_{\Omega_s}\rho p^2\overline{u}_r(r,z,p)\,u^*d\Omega=-\int_{\Omega_s}\overline{F}_r(r,z,p)u^*d\Omega\\
&\int_{\Omega_s}\left(\overline{\sigma}_{zr,r}+\overline{\sigma}_{zz,z}\right)v^*d\Omega+\int_{\Omega_s}\frac{1}{r}\overline{\sigma}_{rz}(r,z,p)v^*d\Omega\\
&\quad-\int_{\Omega_s}\rho p^2\overline{u}_z(r,z,p)\,v^*d\Omega=-\int_{\Omega_s}\overline{F}_z(r,z,p)v^*d\Omega
\end{aligned}
\tag{5}
$$

In view of the Gaussian divergence theorem, one can rewrite the first domain-integral in (5) as

$$
\int_{\Omega_s}\overline{\sigma}_{ab,b}g^*d\Omega=\int_{\partial\Omega_s}\overline{\sigma}_{ab}n_bg^*d\Gamma-\int_{\Omega_s}\overline{\sigma}_{ab}g^*_{,b}d\Omega.
$$

If the test functions $g^*\in\{u^*(\mathbf{x}),\,v^*(\mathbf{x})\}$ are selected as the unit step functions in each subdomain

$$
g^*(\mathbf{x})=\begin{cases}1 & \text{at } \mathbf{x}\in\Omega_s\\ 0 & \text{at } \mathbf{x}\notin\Omega_s\end{cases},
$$

one can rewrite equations (5) into the form

$$
\begin{aligned}
&\int_{\partial\Omega_s}\overline{\sigma}_{rb}n_bd\Gamma+\int_{\Omega_s}\frac{1}{r}\left(\overline{\sigma}_{rr}-\overline{\sigma}_{\varphi\varphi}\right)d\Omega-\int_{\Omega_s}\rho p^2\overline{u}_rd\Omega\\
&\quad=-\int_{\Omega_s}\overline{F}_rd\Omega,\\
&\int_{\partial\Omega_s}\overline{\sigma}_{zb}n_bd\Gamma+\int_{\Omega_s}\frac{1}{r}\overline{\sigma}_{rz}d\Omega-\int_{\Omega_s}\rho p^2\overline{u}_zd\Omega=-\int_{\Omega_s}\overline{F}_zd\Omega
\end{aligned}
\tag{6}
$$

In the MLPG method the test and the trial functions are not necessarily from the same functional spaces. For internal nodes, the test function is chosen as the Heaviside step function with its support on the local subdomain. The trial function, on the other hand, is chosen to be the moving least-squares (MLS) interpolation over a number of nodes randomly spread within the domain of influence (see Fig.2). While the local subdomain is defined as the support of the test function on which the integration is carried out, the domain of influence is defined as a region where the weight function is not zero and all nodes lying inside are considered for interpolation. The approximated function can be written as [Atluri and Shen (2002)]

$$\overline{\mathbf{u}}^h(\mathbf{x},p) = \mathbf{\Phi}^T(\mathbf{x}) \cdot \hat{\mathbf{u}}(p) = \sum_{a=1}^{n} \phi^a(\mathbf{x})\hat{\mathbf{u}}^a(p) \tag{7}$$

where the nodal values $\hat{\mathbf{u}}^a(p)$ are fictitious parameters and $\phi^a(\mathbf{x})$ is the shape function associated with the node a. The number of nodes n used for the approximation of $\overline{u}_i(\mathbf{x},p)$ is determined by the weight function $w^a(\mathbf{x})$. In the present analysis, a 4^{th} order spline-type weight function is chosen as

$$w^a(\mathbf{x}) = \begin{cases} 1 - 6\left(\frac{d^a}{r^a}\right)^2 + 8\left(\frac{d^a}{r^a}\right)^3 - 3\left(\frac{d^a}{r^a}\right)^4 & 0 \le d^a \le r^a \\ 0 & d^a \ge r^a \end{cases} \tag{8}$$

where $d^a = \|\mathbf{x} - \mathbf{x}^a\|$ and r^a is the size of the support domain. It is seen that the C^1 continuity is ensured over the entire domain, therefore the continuity condition of the tractions is satisfied.

Substituting the approximation formula (7) into the stress expressions (3) and subsequently into the local integral equations (6) a system of linear algebraic equations for the unknown fictitious parameters $\{\hat{u}_r, \hat{u}_z\}$ is obtained as

$$\begin{aligned}
&\sum_{\alpha=1}^{n} \hat{u}_r(p) \left\{ \int_{\partial\Omega_s} \left[(2\mu+\lambda)\, n_r \phi^{\alpha}_{,r} + \frac{\lambda}{r} n_r \phi^{\alpha} + \mu n_z \phi^{\alpha}_{,z} \right] d\Gamma \right. \\
&\quad \left. + \int_{\Omega_s} \left[2\mu \left(\phi^{\alpha}_{,r} - \frac{1}{r}\phi^{\alpha} \right) - p^2 \rho \phi^{\alpha} \right] d\Omega \right\} \\
&\quad + \sum_{\alpha=1}^{n} \hat{u}_z(p) \int_{\partial\Omega_s} \left(\lambda n_r \phi^{\alpha}_{,z} + \mu n_z \phi^{\alpha}_{,r} \right)\, d\Gamma \\
&\quad = -\int_{\Omega_s} \overline{F}_r(r,z,p)\, d\Omega, \\
&\sum_{\alpha=1}^{n} \hat{u}_z(p) \left\{ \int_{\partial\Omega_s} \left[(2\mu+\lambda)\, n_z \phi^{\alpha}_{,z} + \mu n_r \phi^{\alpha}_{,r} \right] d\Gamma \right. \\
&\quad \left. + \int_{\Omega_s} \left(\frac{\mu}{r} \phi^{\alpha}_{,r} - p^2 \rho \phi^{\alpha} \right) d\Omega \right\} \\
&\quad + \sum_{\alpha=1}^{n} \hat{u}_r(p) \left\{ \int_{\partial\Omega_s} \left(\mu n_r \phi^{\alpha}_{,z} + \lambda n_z \phi^{\alpha}_{,r} + \frac{\lambda}{r} n_z \phi^{\alpha} \right) d\Gamma \right. \\
&\quad \left. + \int_{\Omega_s} \frac{\mu}{r} \phi^{\alpha}_{,z}\, d\Omega \right\} = -\int_{\Omega_s} \overline{F}_z(r,z,p)\, d\Omega \quad .
\end{aligned} \tag{9}$$

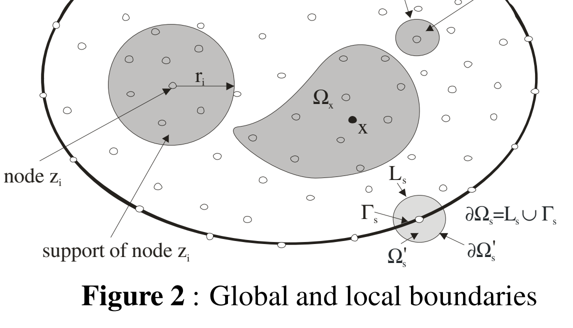

Figure 2 : Global and local boundaries

The local boundary $\partial\Omega_s$ of the local subdomain consists of three parts $\partial\Omega_s = L_s \cup \Gamma_{st} \cup \Gamma_{su}$. Here, L_s is the local boundary that is totally inside the global domain, Γ_{st} is the part of the local boundary which overlaps with the global traction boundary, i.e., $\Gamma_{st} = \partial\Omega_s \cap \Gamma_t$, and similarly Γ_{su} is the part of the local boundary that overlaps with the global displacement boundary, i.e., $\Gamma_{su} = \partial\Omega_s \cap \Gamma_u$ (see Fig. 2). Equations (9) are considered on the subdomains around each interior node and the boundary nodes on Γ_{st}. On the part of the global boundary Γ_{su} with prescribed displacements the approximation formula (7) is collocated at ζ, i.e.,

$$\sum_{\alpha=1}^{n} \phi^{\alpha}(\mathbf{x}) u_b^{\alpha}(p) = \tilde{\overline{u}}_b(\zeta, p) \tag{10}$$

Collecting the discretized LBIEs together with the discretized boundary conditions for the displacements, we get the complete system of linear algebraic equations for the unknown quantities $\{\hat{u}_r, \hat{u}_z\}$.

The time dependent values of the transformed field quantities can be obtained by an inverse Laplace-transform. There are many inversion methods available for the Laplace-transform. In the present analysis, the Stehfest's inversion algorithm [Stehfest (1970)] is applied. Accordingly, an approximate value f_a of the inverse $f(t)$ for a specific time t is given by

$$f_a(t) = \frac{\ln 2}{t} \sum_{i=1}^{N} v_i \overline{f}\left(\frac{\ln 2}{t} i\right) \tag{11}$$

where

$$v_i = (-1)^{N/2+i} \sum_{k=[(i+1)/2]}^{\min(i,N/2)} \frac{k^{N/2}(2k)!}{(N/2-k)!\,k!\,(k-1)!\,(i-k)!\,(2k-i)!} \tag{12}$$

The selected number $N = 10$ with a single precision arithmetic is optimal to receive accurate numerical results. It means that for each time t, it is needed to solve N boundary value problems for the corresponding Laplace-parameters $p = i\ln 2/t$ with $i = 1, 2, ..., N$. If M denotes the number of the time instants in which we are interested to know $f(t)$, then the number of the Laplace-transform solutions $\overline{f}(p_j)$ is $M \times N$.

3 Numerical examples

3.1 Hollow cylinder

A nonhomogeneous and linear elastic hollow cylinder subjected to a static pressure on the internal surface as shown in Fig. 1 is analyzed as a test example. Functionally graded hollow cylinder with a length $L = 0.3$ and radii $a = 4$ and $b = 5$ is investigated. The finite-length cylinder is considered as a part of the infinite-length tube. Hence, the axial displacements on the top and the bottom of the hollow cylinder are assumed to be vanishing. An exponential spatial variation of Young's modulus is chosen as

$$E = E_1 \exp[\beta(r-a)] \tag{13}$$

where $\beta = \frac{1}{b-a}\ln(E_2/E_1)$ with $E_1 = E(a)$ and $E_2 = E(b)$. Poisson's ratio is taken as constant $\nu = 0.25$ and $E_1 = 10^4$. For a homogeneous hollow cylinder, $E(r) = E_1$ and $\beta = 0$. In this case, under the plane strain condition corresponding to an infinite-length tube, an analytical solution is available and it is given by

$$\sigma_{\varphi\varphi} = \sigma_0\left[(b/r)^2 + 1\right] \qquad \sigma_0 = \frac{p}{(b/a)^2 - 1}$$

$$u_r = \frac{\sigma_0}{E_1} r\left[(1+\nu)(b/r)^2 + 1 - \nu\right]. \tag{14}$$

For error and convergence analysis, the following relative percentage errors of L_2-norm are introduced for the radial displacement and the hoop stress as

$$e_u = \frac{\|u^{num} - u^{exact}\|}{\|u^{exact}\|}$$

$$e_s = \frac{\|\sigma^{num} - \sigma^{exact}\|}{\|\sigma^{exact}\|} \tag{15}$$

where

$$\|u\| = \left(\int_\Omega (u_r)^2 d\Omega\right)^{1/2} \qquad \|\sigma\| = \left(\int_\Omega (\sigma_{\varphi\varphi})^2 d\Omega\right)^{1/2}$$

The relative percentage errors and the convergence rates for three different node distributions are presented in Fig. 3, where s represents the node-distance. The accuracy is very high especially for the finest node distribution consisting of 105 (21x5) nodes uniformly distributed in the rectangular domain with 21 nodes in the radial direction. In other two cases, 44 (11x4) and 24 (6x4) nodes have been used.

Next, the influence of the gradation of the material properties on the radial displacements and the hoop stresses is analyzed. In Figs. 4 and 5 the following notation is used: $u_1 = u_r(a)$, $u_2 = u_r(b)$, $s_1 = \sigma_{\varphi\varphi}(a)$ and $s_2 = \sigma_{\varphi\varphi}(b)$. Numerical results provided by the MLPG method are compared with those obtained by the FEM-code MSC/NASTRAN. Axisymmetric triangular elements with a quadratic approximation have been used in the FEM analysis. In the FEM calculations, 100 elements in the radial direction and 10 elements in the axial direction, with a total number of 1000 elements for the rectangular cross-section of the hollow cylinder with the axial plane. A good agreement between both results is achieved, which verifies the accuracy of the present meshless method. For convenience, the radial displacements are normalized by $u_r(a)$ and the hoop stresses by $\sigma_{\varphi\varphi}(a)$.

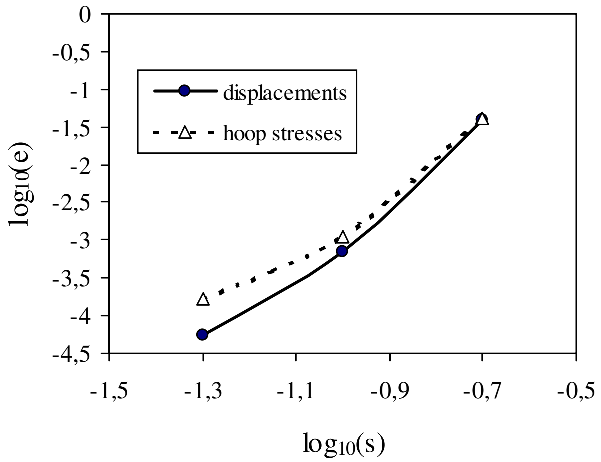

Figure 3 : Relative errors and convergence rates

The hollow cylinder under an impact load $\sigma_{rr}(t) = pH(t-0)$ on the internal surface of the hollow cylinder is analyzed too. The same material constants as in the previous static case are chosen. The mass density is taken as $\rho = 500$.

The time variations of the radial displacement on the internal surface of the hollow cylinder are shown in Figs. 6 and 7 for two different gradient parameters of Young's modulus. A node distribution consisting of 105 (21x5) nodes uniformly distributed in the rectangular domain is used for our MLPG analysis. In the FEM analysis, the same mesh as in the previous static analysis is used now. The time step is selected as 0,0002. A very good agreement between the FEM and the MLPG results is obtained. It verifies again the accuracy of the present method. In the FGM hollow cylinder with a gradually increasing Young's modulus in the radial direction characterized by $E_2/E_1 = 5.$, the frequency of the oscillations is higher as compared to that in a homogeneous hollow cylinder, but the amplitude is decreased. The opposite phenomena are observed in Fig. 7, where Young's modulus is gradually decreasing with radial coordinate. The radial displacements on the external surface of the hollow cylinder are presented in Figs. 8 and 9. The difference between the displacements on the internal (A) and external surfaces (B) is negligible in the investigated case.

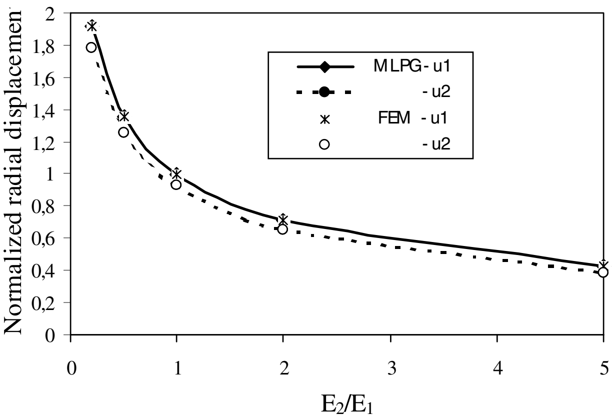

Figure 4 : Variation of the normalized radial displacement with the nonhomogeneity ratio E_2/E_1

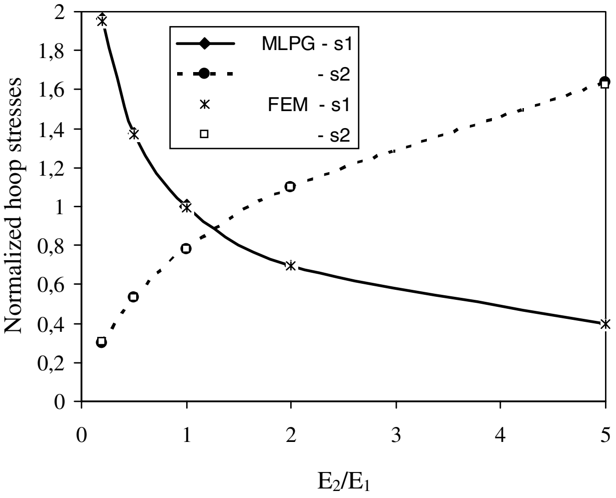

Figure 5 : Variation of the normalized hoop stress with the nonhomogeneity ratio E_2/E_1

Figures 10 and 11 show the time variations of the hoop stresses on the internal surface of the hollow cylinder for the material gradations $E_2/E_1 = 5., 0.2$, respectively. In contrast to the displacement variations, the FEM results for hoop stresses show a non-smooth behavior. This is due to the fact that in MSC NASTRAN-code the material properties are assumed to be uniform within each element. Numerical results for a homogeneous and an FGM hollow cylinder are given here to analyze the influence of the material gradation on the variation of the hoop stresses. Figure 10 shows that if Young's modulus is gradually increasing with radial coordinate the hoop

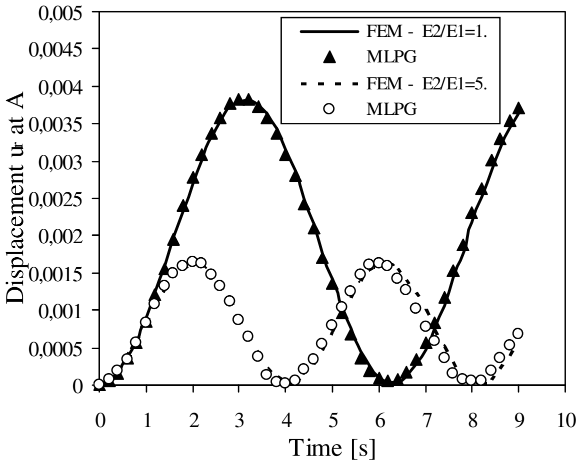

Figure 6 : Time variation of the radial displacement on the internal surface of the FGM cylinder for$E_2/E_1 = 5$.

stress at the internal surface is significantly reduced compared to that in a homogeneous cylinder. It should be noted here that the same values of Young's modulus on the internal surface are used in both homogeneous and FGM hollow cylinders. Higher values of hoop stresses are observed on the external surface of the cylinder as can be seen in Fig. 12.

It is interesting to understand the influence of the mass density on the time variation of the hoop stresses. For this purpose, we have investigated the case where the Young's modulus and the mass density have the same exponential variation according to Eq. (13). The corresponding numerical results are given in Fig. 13. Since both material parameters have the same spatial variation, the velocity of the wave propagation is constant in the whole cylinder. Thus, the peaks of the hoop stresses should appear at the same time instants as in the homogeneous case (i.e., uniform or constant Young's modulus and mass density), denoted here by a dashed line. Figure 13 verifies that the peak hoop stresses for a constant and a variable mass density under the same Young's modulus variation are almost the same in both cases. This implies that the mass density has a minimal influence on the peak values of the hoop stresses, at least in the case considered here. The peak hoop stresses are mainly influenced by the variation of Young's modulus. In Fig. 13, numerical results for a uniform mass density and an exponentially graded

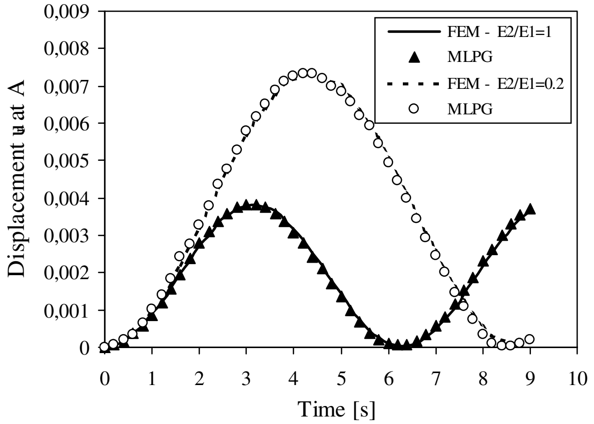

Figure 7 : Time variation of the radial displacement on the internal surface of the FGM cylinder for$E_2/E_1 = 0.2$

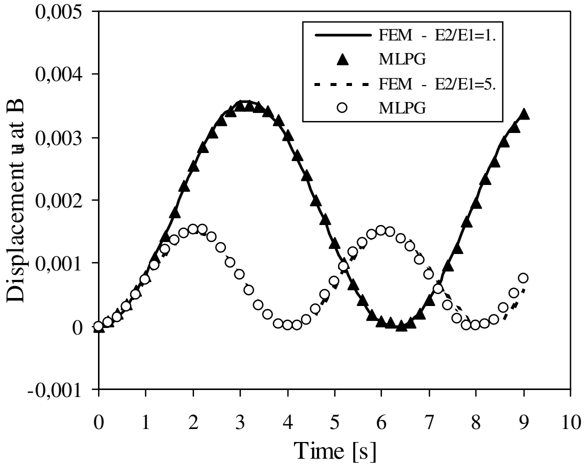

Figure 8 : Time variation of the radial displacement on the external surface of the FGM cylinder for$E_2/E_1 = 5$.

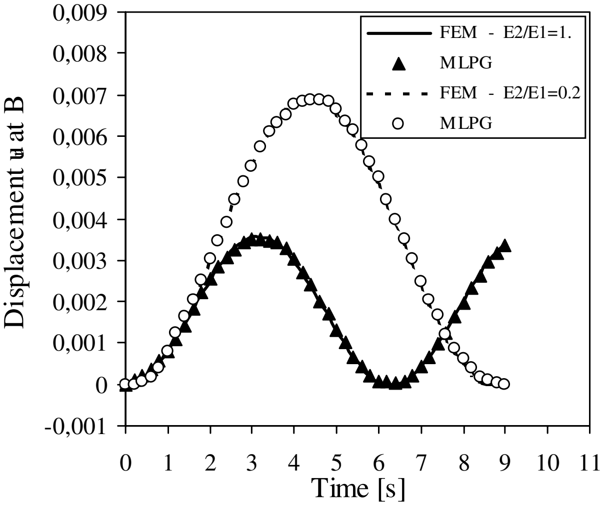

Figure 9 : Time variation of the radial displacement on the external surface of the FGM cylinder for$E_2/E_1 = 0.2$

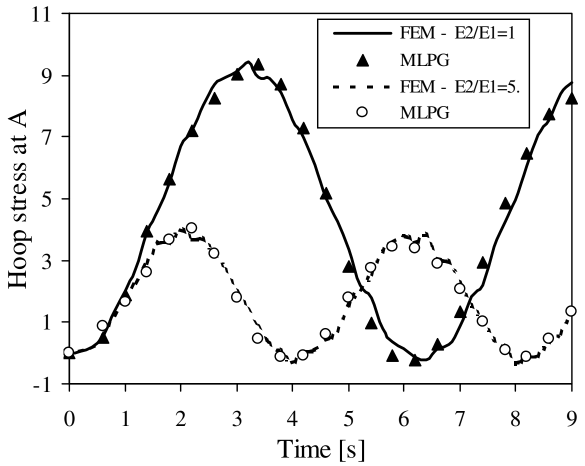

Figure 10 : Time variation of the hoop stresses on the internal surface of the FGM cylinder for$E_2/E_1 = 5$.

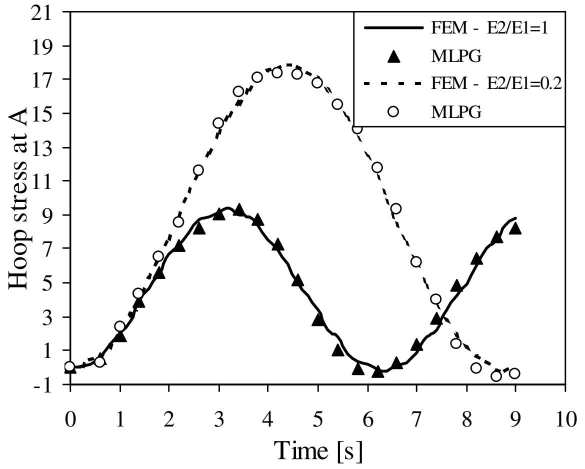

Figure 11 : Time variation of the hoop stresses on the internal surface of the FGM cylinder for$E_2/E_1 = 0.2$

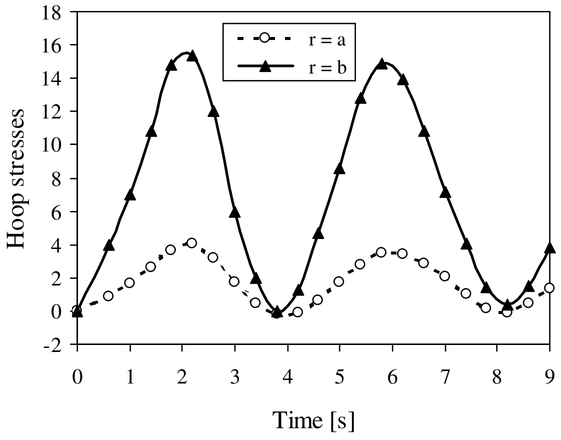

Figure 12 : Time variation of the hoop stresses on both surfaces of the FGM cylinder for$E_2/E_1 = 5$.

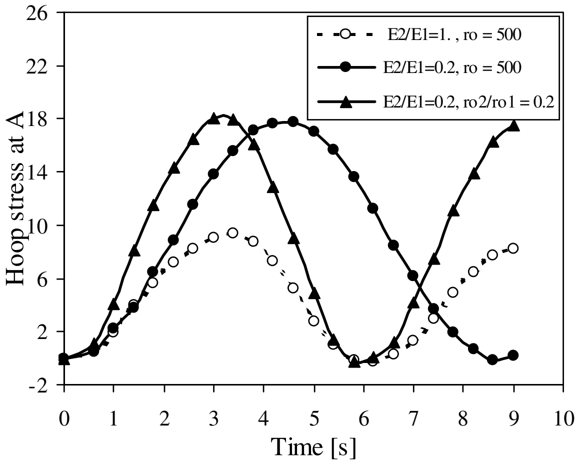

Figure 13 : Influence of the mass density variation on the hoop stress at internal surface of the FGM hollow cylinder

mass density are compared, assuming the same exponential variation of the Young's modulus with $E_2/E_1 = 0.2$. In the former case (solid line with full circles) the velocity of the wave propagation is lower than in the latter case.

3.2 A penny-shaped crack in a finite cylinder

In the last numerical example a penny-shaped crack in a finite cylinder as depicted in Fig. 14 is analyzed. The following geometry is considered: crack radius$a = 0.5$, cylinder radius $w = 1.$, and cylinder length $L = 0.3$. The penny-shaped crack is located at the center of the cylinder which is subjected to a uniform tension $\sigma = 1.$, or to a fixed-grip loading with a prescribed uniform static deformation ε_0. Also in this example, an exponential spatial variation of Young's modulus is assumed

$$E = E_0 \exp[\beta(r-a)].$$

Poisson's ratio is taken as constant $\nu = 0.25$, and the Young's modulus at the crack-front is selected as $E_0 = 10^4$. It means that Young's moduli at the crack-front in the homogeneous and the FGM cylinders are chosen as the same. A regular node distribution with 930 (31x30) nodes is used for the MLS approximation of the displacements in the analyzed domain ABCDE (see Fig.14).

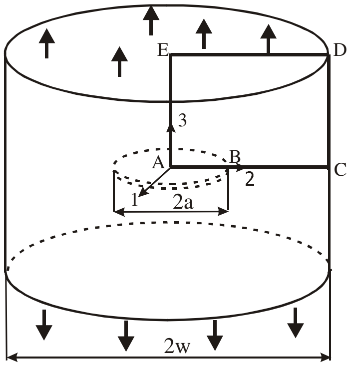

Figure 14 : A penny-shaped crack in a finite cylinder

Though there are many established methods available for computing the stress intensity factors, we apply in this analysis a simple approach based on the extrapolation technique following directly from the asymptotic expansion of the stresses or displacements in the vicinity of the crack-front. For homogeneous and linear elastic solids, Sih et al. (1972) have shown that the dynamic stress intensity factors can be conventionally extracted from the dynamic crack-tip stress field in the Laplace-transformed domain. Since the spatial distribution of the Laplace-transform of the asymptotic stresses is the same as in the case of a static loading, it is only necessary to invert the Laplace-transform of the stress intensity factors. For non-homogeneous solids, Eischen (1987) has shown that the asymptotic crack-tip stress and displacement fields have the same form as those in homogeneous materials. Although the spatial distribution of the asymptotic crack-tip fields is not influenced by the material gradient parameters in FGMs and the temporal variation of the dynamic loading, the stress intensity factors are dependent on both material gradation and time, through the elastic solution of the initial-boundary value problems of the cracked solid. The elastodynamic stress intensity factors are related to the crack-opening-displacements by

$$\begin{Bmatrix} K_I(t) \\ K_{II}(t) \\ K_{III}(t) \end{Bmatrix} = \frac{\sqrt{2\pi}}{4(1-\nu)}\mu(a,\varphi)\lim_{\delta\to 0}\frac{1}{\sqrt{\delta}}$$

$$= \begin{Bmatrix} \Delta u_\zeta(\delta,t) \\ \Delta u_\xi(\delta,t) \\ (1-\nu)\Delta u_\eta(\delta,t) \end{Bmatrix} \tag{16}$$

where $K_I(t)$, $K_{II}(t)$, and $K_{III}(t)$ are the time-dependent mode-I, mode-II and mode-III dynamic stress intensity factors, $\mu(a,\varphi)$ is the local shear modulus at the crack-front, δ is a small distance of a node on the crack-surface to the crack-front, and $\Delta u_\xi(\delta,t)$, $\Delta u_\eta(\delta,t)$ and $\Delta u_\zeta(\delta,t)$ are the crack-opening-displacements in the local coordinate system (ξ,η,ζ) at the crack-front, respectively. In the local coordinate system, ξ is normal and η is tangential to the crack-front, while ζ is perpendicular to the (ξ,η)-plane. In the extrapolation technique, Eq. (16) is used for computing the dynamic stress intensity factors.

To test the proposed method, a penny-shaped crack in an FGM cylinder under a uniform static tensile load is first considered. In this loading case, only the mode-I stress intensity factor occurs, while the mode-II and the mode-III stress intensity factors are identically zero. Numerical results for the normalized mode-I stress intensity factors $f_I = K_I/\sigma\sqrt{\pi a}$ and $f_I = K_I/E_0\varepsilon_0(1-\nu^2)\sqrt{\pi a}$ for a uniform stress and fixed-grip loading, respectively, and various values of the material gradation exponent β are given in Tab. 1. For a negative value of the gradation exponent β the axial stresses at the axis of the cylinder are higher in the fixed-grip loading case than in the uniform stress loading case. An opposite phenomena is observed for positive values of β. Therefore, stress intensity factors (SIFs) for negative values of β are higher for fixed-grip loading case than for a uniform stress loading case. However, the difference is not significant in the investigated case because of the considered geometry $a/w = 0.5$ and the exponential gradation originating at the crack-front. The normalized stress intensity factors are given in Table 1, which shows a good agreement with the FEM results for both loading cases. The relative error of the stress intensity factors for a penny-shaped crack in a homogeneous cylinder is 2,5%, with reference to the result given by Murakami (1987).

Table 1 : Stress intensity factors for a penny-shaped crack in a finite FGM cylinder

β	f_I Uniform stress load		f_I Fixed-grip load	
	MLPG	FEM	MLPG	FEM
0	0.652	0.665	0.63	0.64
0.5	0.59	0.598	0.539	0.55
1.	0.528	0.535	0.455	0.468
-1.	0.82	0.819	0.86	0.854

A circumferential crack with a ratio $a/w = 0.5$ is analyzed too. By using the same node distribution as for a penny-shaped crack, the relative error of the stress intensity factor for a circumferential crack in a homogeneous cylinder with reference to the result of Murakami (1987) is 2,1%.

Numerical results for a penny-shaped crack in a homogeneous linear elastic cylinder under an impact loading are presented in Fig. 15. Our results are compared with the FEM results. A quite good agreement between both results is observed there. Figure 16 shows the time variation of the mode-I dynamic stress intensity factor for a penny-shaped crack in an FGM cylinder. Numerical calculations are carried out for a constant mass density $\rho = 500$ and agradation exponent $\beta = -1$. On the external surface of the cylinder the Young's modulus is lower than at the center, and its value at the crack-front is taken as the same as in the homogeneous cylinder. Since the crack radius is a half of the cylinder radius, the time needed for the elastic waves traveling from the cylinder center to the outer surface is almost the same as in the homogeneous case, despite that the wave velocity is varying in radial direction due to the variation of the Young's modulus. Therefore, the peak values of the dynamic stress intensity factor for the homogeneous and the FGM cylinders appear nearly at the same time instants. To analyze the influence of the variation of the Young's modulus, the dynamic SIF for homogeneous and FGM cylinders are given and compared in Fig. 16. Figure 16 implies that for a decreasing Young's modulus in the radial direction, the peak dynamic stress intensity factor is increased, which is unfavorable from the point of view of linear elastic fracture mechanics. For an increasing Young's modulus in the radial direction, an opposite conclusion is expected.

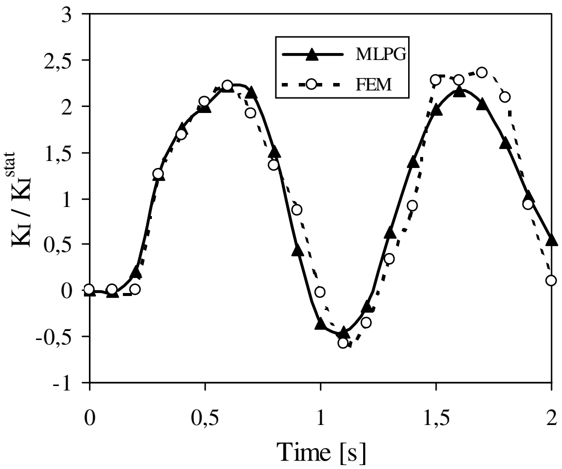

Figure 15 : Time variation of the stress intensity factor for a penny-shaped crack in a homogeneous cylinder

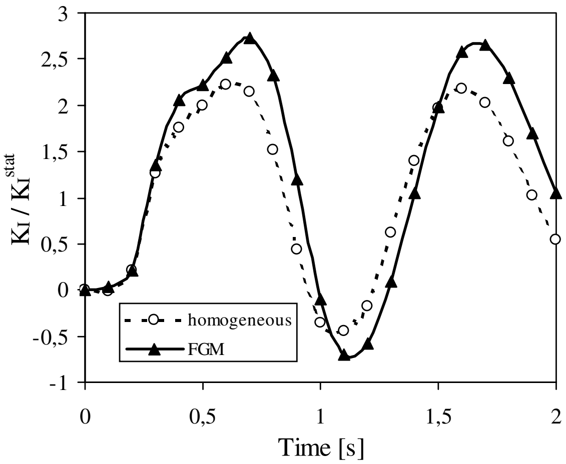

Figure 16 : Time variation of the stress intensity factor for a penny-shaped crack in an FGM cylinder with $\beta = -1$

4 Conclusions

The essential results of the present as follows:

A local boundary integral equation formulation based on the MLPG in the Laplace-transformed domain with a meshless approximation has been successfully implemented to solve 3-d axisymmetric problems in isotropic continuously nonhomogeneous and linear elastic solids subjected to static and dynamic loads.

A unit step function is used as the test function in the local symmetric weak-form. The derived local boundary-domain integral equations are non-singular. Axial symmetry of the geometry and the boundary conditions for a 3-d body reduces the original 3-d boundary value problem into a 2-d problem. The analyzed domain is divided into small overlapping circular sub-domains on which the local boundary integral equations are applied. The proposed method is a truly meshless method, which requires neither elements nor background cells in either the interpolation or the integration.

The proposed method yields a pure contour-integral method for static boundary value problems even for nonhomogeneous material properties. The efficiency and the adaptability of the present method is high in the sense that a mesh generation is not needed.

One of the main drawbacks of the conventional BEM, namely the limitation of its applications to homogeneous solids, can be circumvented by using the present method. The method does not require the fundamental solutions, which are either not available or too complicated for continuously nonhomogeneous solids. The computational accuracy of the present method is comparable with that of FEM.

Acknowledgement: The authors acknowledge the support by the Slovak Science and Technology Assistance Agency registered under the project number APVT-51-003702, the Slovak Grant Agency VEGA-2303823, and the project jointly supported by the German Academic Exchange Service (DAAD) and the Ministry of Education of Slovak Republic under the project number D/04/25722.

References

Atluri, S. N.; Shen, S. (2002): *The Meshless Local Petrov-Galerkin (MLPG) Method*, Tech Science Press.

Atluri, S. N. (2004): *The Meshless Method , (MLPG) For Domain & BIE Discretizations*, Tech Science Press.

Atluri, S.N.; Sladek, J.; Sladek, V.; Zhu, T. (2000): The local boundary integral equation (LBIE) and its meshless implementation for linear elasticity. *Comput. Mech.*, 25: 180-198.

Atluri, S.N.; Han, Z.D.; Shen, S. (2003): Meshless local Petrov-Galerkin (MLPG) approaches for solving the weakly-singular traction & displacement boundary integral equations. *CMES: Computer Modeling in Engineering & Sciences*, 4: 507-516.

Belytschko, T.; Lu, Y.; Gu, L. (1994): Element free Galerkin methods. *Int. J. Num. Meth. Engn.*, 37: 229-256.

Belytschko, T.; Krogauz, Y.; Organ, D.; Fleming, M.; Krysl, P. (1996): Meshless methods; an overview and recent developments. *Comp. Meth. Appl. Mech. Engn.*, 139: 3-47.

Cruse, T.; Snow, D.W.; Wilson, R.B. (1977): Numerical solutions in axisymmetric elasticity, *Computers & Structures,* 7: 445-451.

Eischen, J.W. (1987): Fracture of nonhomogeneous materials, *Int. J. Fracture*, 34: 3-22.

Han, Z.D.; Atluri, S.N. (2004a): Meshless local Petrov-Galerkin (MLPG) approaches for solving 3D problems in elasto-statics. *CMES: Computer Modeling in Engineering & Sciences*, 6: 169-188.

Han, Z.D.; Atluri, S.N. (2004b): A meshless local Petrov-Galerkin (MLPG) approach for 3-dimensional elasto-dynamics. *CMC: Computers, Materials & Continua*, 1: 129-140.

Kermanidis, T.A. (1975): A numerical solution for axially symmetrical elasticity problems, *Int. J. Solids and Structures*, 11: 493-500.

Lacerda, L.A.; Wrobel L.C. (2001): Hypersingular boundary integral equation for axisymmetric elasticity. *Int. J. Num. Meth. Engn.*, 52: 1337-1354.

Mikhailov, S.E. (2002): Localized boundary-domain integral formulations for problems with variable coefficients. *Engn. Analysis with Boundary Elements*, 26: 681-690.

Murakami, Y. (1987): *Stress Intensity Factor Handbook*, Pergamon Press.

Sellountos, E.J.; Polyzos, D. (2003): A MLPG (LBIE) method for solving frequency domain elastic problems, *CMES: Computer Modeling in Engineering & Sciences*, 4: 619-636.

Sellountos, E.J.; Vavourakis, V.; Polyzos, D. (2005): A new singular/hypersingular MLPG (LBIE) method for 2D elastostatics, *CMES: Computer Modeling in Engineering & Sciences*, 7: 35-48.

Sih, G.C.; Ravera, R.S.; Embley, G.T. (1972): Impact response of a finite crack in plane extension, *Int. J. Solids Structures*, 8: 977-993.

Sladek, J.; Sladek, V.; Atluri, S.N. (2000): Local boundary integral equation (LBIE) method for solving problems of elasticity with nonhomogeneous material properties. *Computational Mechanics,* 24: 456-462.

Sladek, J.; Sladek, V.; Van Keer, R. (2003a): Meshless local boundary integral equation method for 2D elastodynamic problems. *Int. J. Num. Meth. Engn.*, 57: 235-249

Sladek, J.; Sladek, V.; Zhang, Ch. (2003b): Application of meshless local Petrov-Galerkin (MLPG) method to elastodynamic problems in continuously nonhomogeneous solids, *CMES: Computer Modeling in Engn. & Sciences*, 4: 637-648.

Stehfest, H. (1970): Algorithm 368: numerical inversion of Laplace transform. *Comm. Assoc. Comput. Mach.*, 13: 47-49.

Suresh, S.; Mortensen, A. (1998): *Fundamentals of Functionally Graded Materials*. Institute of Materials, London.